# The PXBAR-domain protein SNX9 selectively sequesters PI(3,4)$P_2$ lipid and protects it from hydrolysis at the plasma membrane

Jeriann R. Beiter,[1] Chieh-Ju Sung,[2] Shan-Shan Lin,[2] Nicolas de Vuono,[3] Senthil Arumugam,[4] John Manzi,[3] Aurélie Bertin,[3] Patricia Bassereau,[3] Ya-Wen Liu,[2*] Gregory A. Voth,[1*] Feng-Ching Tsai[3]*

[1] Department of Chemistry, Chicago Center for Theoretical Chemistry, Institute for Biophysical Dynamics, and James Franck Institute, The University of Chicago, Chicago, IL 60637, USA

[2] National Taiwan University College of Medicine, Institute of Molecular Medicine, TW.

[3] Institut Curie, Université PSL, Sorbonne Université, CNRS UMR168, Physique des Cellules et Cancer, 75005 Paris, FR.

[4] European Molecular Biological Laboratory Australia (EMBL Australia) and Monash Biomedicine Discovery Institute, Faculty of Medicine, Nursing and Health Sciences, Monash University, Clayton/Melbourne, AU.

* Corresponding authors: feng-ching.tsai@curie.fr; gavoth@uchicago.edu; yawenliu@ntu.edu.tw

## ABSTRACT

The phosphoinositidyl lipid (PIP) family is key to spatial regulation of cellular processes, and their appearance, disappearance, and interconversion provide key signals for membrane remodeling at the plasma membrane and beyond. These signals are connected to recruitment of various peripheral membrane proteins, including sorting nexin 9 (SNX9), an important regulator of late stage endocytic and macropinocytic remodeling. Using a combination of live cell imaging, *in vitro* reconstitution, and atomistic molecular dynamics simulation, we probe the question of whether SNX9 is selective for PI(3,4)$P_2$ over PI(4,5)$P_2$, and what the physiological implications of this selectivity may be. We find that SNX9 recruitment to the plasma membrane is coincident with PI(3,4)$P_2$ but not PI(4,5)$P_2$ during macropinocytic ruffle maturation, and that SNX9 differentially remodels GUVs containing PI(3,4)$P_2$ over PI(4,5)$P_2$. Atomistic simulations further corroborate these findings and suggest that the primary mediator of this difference is a non-canonical binding interface in the fourth helix of the PX domain, which is further probed with mutational assays. We therefore hypothesize that SNX9 binding to PI(3,4)$P_2$ over PI(4,5)$P_2$ not only helps with modulating the spatiotemporal recruitment of SNX9 during plasma membrane remodeling processes, but also acts as a check to prevent the premature conversion of PI(3,4)$P_2$ into PI(3)P, thus acting as a regulator of these processes.

## TEASER

A physical and molecular basis for the retention of pre-endosomal identity for coordination of pre-scission events.

## INTRODUCTION

Cells rely on the dynamic and localized synthesis of phosphoinositide (PIP) lipids to generate specialized membrane regions that recruit PIP-associated proteins at precise locations and times. This intricate PIP synthesis regulation enables numerous membrane processes, especially in endocytic pathways, such as clathrin-mediated and clathrin-independent endocytosis, macropinocytosis, phagocytosis, and pinocytosis. During these endocytic processes, specific kinases and phosphatases catalyze PIPs to produce different PIP species sequentially. For example, in macropinocytosis, the enrichment of PIPs starts from PI(4,5)$P_2$ to PI(3,4,5)$P_3$, then PI(3,4)$P_2$, and finally PI(3)P, a marker of early endosomal membranes(*1-3*). Similarly, clathrin-mediated endocytosis beings with PI(4,5)$P_2$ enrichment, followed by PI(3,4)$P_2$, and then PI3P (as reviewed in (*4, 5*)). PI(4,5)$P_2$ is known to be abundant at the plasma membrane, where its local concentration often increases during endocytosis. In contrast, other PIPs like PI(3,4)$P_2$ are synthesized transiently and at much lower concentrations at endocytic sites, with PI(3,4)$P_2$ level being ~ 40-fold lower than PI(4,5)$P_2$(*6*). To recognize and bind specific PIP lipids, many membrane-associated proteins have PIP-binding domains such as PX (phox homology), PH (pleckstrin homology), FYVE (Fab1, YOTB, Vac1 and EEA1), and C2 domains (reviewed in (*7*)). These domains often display affinity for multiple PIPs species. For instance, various PX domains bind both PI(4,5)$P_2$ and PI(3,4)$P_2$, though with different affinities(*8*). Discriminating between similar PIPs, such as PI(3,4)$P_2$ and PI(4,5)$P_2$, is challenging due to their nearly identical headgroups, which share the same charges, sizes, and protonation constants (Fig. 1)(*9, 10*). This overlapping specificity of similar PIPs raises fundamental questions: How do protein domains achieve selective recognition of specific PIP lipids? How might PIP-binding proteins impact PIP conversions, possibly by affecting phosphatase accessibility and thus modulating endocytic processes? Addressing these questions is fundamental for deciphering the regulation of membrane dynamics in cells.

The crystal structures of PIP-associated domains typically reveal a single PIP bound in a canonical binding pockets(*11-14*). However, there is growing evidence that many protein domains interact with lipids in a promiscuous, multivalent manner(*15, 16*). Superstoichiometric lipid binding, where one protein domain can simultaneously bind multiple lipids of the same species, often involves additional secondary binding pockets or polybasic patches and motifs that promote such interactions(*16-18*). For instance, recent molecular dynamics (MD) simulations have shown that domains like the FERM domain of ezrin can bind simultaneously to multiple PI(4,5)$P_2$ lipids, and the PH domain of GRP1, with at least two $PIP_3$ lipids (*19-21*). PIP phosphatases and kinases, have highly specialized domains that use a combination of electrostatic and steric effects to achieve selectivity, occasionally in combination with other peripheral PIP binding domains, as reviewed in (*22*). In contrast, other peripheral membrane proteins containing PH and PX domains are relatively weak binders yet still exhibit certain PIP selectivity(*8, 23*). How protein domains achieve superstoichiometric yet selective PIP binding remains an open question in understanding the molecular mechanisms of lipid-protein interactions.

In this study, to reveal how certain proteins achieve both superstoichiometric and selective PIP binding, we investigated how the PX domain of sorting nexin 9 (SNX9) interacts with PI(4,5)P2 and PI(3,4)P2, two key PIP lipids in SNX9-mediated endocytosis and macropinocytosis. SNX9 consists of an N-terminal Src Homology 3 (SH3) domain, a long unstructured motif termed the "low complexity" (LC) domain, and a C-terminal PX-BAR unit,

which comprises a PX domain paired with a Bin/Amphiphysin/Rvs (BAR) domain (Fig. 1). BAR domains are known to bind to negatively charged lipids, including PIPs and phosphoserine (PS) lipids; moreover, many BAR domains have been shown to be able to sense and generate curved membranes(*24*). SNX9 has been shown to play a prominent role in clathrin-mediated endocytosis and micropinocytosis, by facilitating plasma membrane deformation and by recruiting partners such as dynamin and actin nucleation promoting factor N-WASP(*25, 26*). While SNX9's PX domain is thought to assist in targeting PIP-rich membranes, its PIP binding selectivity remains unclear. Many studies have investigated SNX9's PIP preference: some indicate PI(3,4)$P_2$ and PI(4,5)$P_2$ as predominant, while others suggest a preference for PI3K products such as PI(3)P, PI(3,4)$P_2$, and $PIP_3$ (*8, 27, 28*). Other work indicates that SNX9 binds both PI(3,4)$P_2$ and PI(4,5)$P_2$ weakly, and is recruited to membranes through a general electrostatic mechanism(*29*). While the high resolution SNX9 PX-BAR crystal structure indicates the binding of the short-chain PI(3)P to the canonical binding pocket of the PX domain, it does not clarify selective binding mechanism for other $PIP_2$ lipids (PDB ID: 2RAK(*11*). Unlike PI(3)P, which has a smaller charged headgroup, the more complex $PIP_2$ headgroups suggest that electrostatic and steric factors might allow the PX-BAR domain to achieve specific PIP binding, particularly with the additional consideration fo superstoichiometric lipid binding.

In this study, we conduct live-cell imaging to quantify the temporal recruitment of SNX9 in relation to PIP enrichment in macropinocytic membrane ruffles, revealing a synchronous recruitment with PI(3,4)$P_2$ and a delayed recruitment relative to PI(4,5)$P_2$. Using *in vitro* reconstituted assays, we further find that SNX9 binds to PI(3,4)$P_2$ or PI(4,5)$P_2$ with comparable affinities, and SNX9 can generate and sense membrane curvature regardless of the PIP2 species. To reveal how SNX9 affects the dynamics of PI(4,5)$P_2$ and PI(3,4)$P_2$ at the molecular scale, we perform atomistic MD simulations of SNX9 PX-BAR domain with model membranes. Our simulation uncovered a non-canonical binding interface within the PX domain that promote PI(3,4)$P_2$ selectivity over PI(4,5)$P_2$. We hypothesize that this selective sequestering may impact PI(3,4)$P_2$ conversion during macropinocytosis. By performing mutational analysis in cells, we validate that this non-canonical interface can interfere in the ability of the downstream phosphatase INPP4B in converting PI(3,4)$P_2$ into PI3P. Collectively, our findings suggest that the ability of SNX9 to selectively sequester PI(3,4)$P_2$ may not only facilitate its recruitment to the plasma membrane, but also offer a "protective" effect, potentially preventing PI(3,4)$P_2$ from being prematurely converted into PI(3)P during macropinocytosis and endocytosis.

## RESULTS

### SNX9 recruitment is coincident with PI(3,4)$P_2$ production but not PI(4,5)$P_2$

To investigate the interplay between SNX9 and PI(4,5)P2 or PI(3,4)P2 during micropinocytosis, we conducted live-cell imaging to monitor their spatiotemporal distribution upon stimulation with platelet-derived growth factors (PDGF) in serum-starved cells. The initial stage of micropinocytosis involves membrane ruffle formation, a process where SNX9 plays a crucial role (*30*). We performed time-lapse imaging of cells overexpressing fluorescently tagged SNX9 alongside fluorescent PH-domain probes for PI(4,5)$P_2$ (PLCδ-PH-EGFP) or PI(3,4)$P_2$ (NES-EGFP-cPHx3) to track the recruitment and dynamics of each

molecule at the sites of ruffle formation (Fig. 2, A and D). Our results show that SNX9 co-localizes spatially with both PIP2 reporters at PDGF-induced membrane ruffles (Fig 2, B and E). However, quantitative analysis of SNX9 and $PIP_2$ fluorescence intensity profiles during the first 60 seconds of ruffle formation shows distinct enrichment kinetics (Fig 2). Specifically, for $PI(4,5)P_2$, we observe a delayed appearance of SNX9 fluorescence relative to $PI(4,5)P_2$ at the same membrane ruffle site (Fig. 2C). In contrast, SNX9 and $PI(3,4)P_2$ fluorescence signals appear simultaneously, with no detectable lag (Fig. 2F). Statistical analysis confirms no significant difference in the relative signal intensities of SNX9 and $PI(3,4)P_2$ at any time point, suggesting synchronous recruitment. The observed delayed, yet spatially colocalized, appearance of SNX9 relative to $PI(4,5)P_2$ is consistent with the established role of $PI(4,5)P_2$ as an upstream factor during endocytosis and macropinocytosis(*1*). However, the simultaneous appearance of SNX9 with $PI(3,4)P_2$, as opposed to the lag observed with PI(4,5)P2, suggests a potential selective association between SNX9 and $PI(3,4)P_2$ at macropinocytic ruffles. Our finding suggests that PI(3,4)P2 may preferentially recruit SNX9, indicating a specificity of SNX9 for $PI(3,4)P_2$ over $PI(4,5)P_2$. This observation aligns with previous reports that PI(3,4)P2 facilitates selective SNX9 recruitment at the late stage of clathrin-mediated endocytosis, facilitating the recruitment of dynamin by SNX9 to drive membrane fission(*29, 31*).

**SNX9 senses and generates membrane curvature for both $PI(3,4)P_2$- and $PI(4,5)P_2$-containing membranes**

Given that SNX9 is a BAR domain protein, we next ask how different PIP species in membranes impacts the expected ability of SNX9 to sense and generate curved membranes. We purified full length SNX9 and labelled it with Alexa fluorophore dyes for detection by confocal microscopy. We first determine whether SNX9's binding affinity to flat membranes differs between $PI(4,5)P_2$ and $PI(3,4)P_2$. To do this, we use giant unilamellar vesicles (GUVs) with diameters of about 5 μm or larger. GUV membranes were composed of eggPC, supplemented with 10 mol% DOPS, 10 mol% DOPE, 15 mol% cholesterol, and 0.5 mol% Bodipy ceramide, along with either 8 mol% $PI(4,5)P_2$ or $PI(3,4)P_2$. Upon incubating SNX9 with GUVs, we observed the formation of outward membrane tubules on the GUVs, confirming SNX9's ability to deform and generate membrane tubules, a characteristic feature of BAR domains (Fig 3, A and B). To estimate the binding affinities of SNX9 on $PI(4,5)P_2$- and $PI(3,4)P_2$-containing GUVs, we measured the surface density of SNX9 on GUV membranes as a function of its bulk concentration (Fig. 3, C and D)(*32*). By fitting to the Hill equation, we estimated dissociation constants of 31 nM for $PI(4,5)P_2$ and 47 nM for $PI(3,4)P_2$. These comparable affinities are consistent with previous findings for the PX-BAR domain of SNX9 on small unilamellar vesicles (*29*).

To evaluate the membrane curvature sensing ability of SNX9, we generated cylindrical membrane nanotubes from SNX9-coated GUVs using optical tweezers (Fig. 3E). We quantified the enrichment of SNX9 on the nanotubes relative to the flat GUV membranes, calculating the sorting ratio as previously described for other BAR domains. Our results show that SNX9's sorting ratio increases when the membrane tubes are thinner, within the experimentally accessible curvature range of ~ 0.0125 $nm^{-1}$ to ~ 0.15 $nm^{-1}$ (tubes with radii of 80 nm and 7 nm, respectively) (Fig. 3F). By comparing the sorting ratio of SNX9 at a relatively

low surface density, less than 400 $\mu m^{-2}$ (about 2% surface coverage), where relative enrichment is expected to be the most significant, we observe no significant difference in sorting ratios between $PI(4,5)P_2$ and $PI(3,4)P_2$ (Fig. 3F). To obtain the effective spontaneous curvature of SNX9, which indicates how much the protein deforms membranes locally, we performed analysis as previously performed (see materials and methods for details). The spontaneous curvatures are comparable for $PI(4,5)P_2$ and $PI(3,4)P_2$ containing membranes, ~ 7 nm and ~ 11 nm, respectively. These findings indicate that the mechanical effect of SNX9 on membranes is similar with $PI(4,5)P_2$ and $PI(3,4)P_2$, as revealed at macroscopic scale.

To gain molecular-scale insights into how SNX9 organizes and deforms $PI(4,5)P_2$- and $PI(3,4)P_2$-containing membranes, we performed cryo-electron microscopy (cryo-EM). A heterogeneous solution of Large Unilamellar Vesicles (LUVs), with diameters varying from 50 nm to 1 μm was prepared by resuspending dry lipid films composed of DOPC and 15% DOPS, supplemented with 10% $PI(4,5)P_2$ or $PI(3,4)P_2$. Tubulated liposomes can also be obtained through this process (about 15% of liposomes). These liposomes were incubated with 1 μM SNX9 for at least 1 hour at room temperature before being plunge frozen onto EM grids. Our cryo-EM results revealed dense SNX9 binding on membrane tubes under both PIP conditions with a lower density on the rest of the vesicles (Figs. 4A-B). However, unlike previous studies where BAR domains displayed well-registered alignment on membrane tubes, SNX9 exhibits a disorganized binding on tubes (Fig. 4, arrows)(*33*). This difference in organization suggests that the full-length SNX9, with its disordered regions, organizes less regularly on membrane tubes. The median diameters of SNX9 decorated tubes, 11.4 nm for membranes containing $PI(3,4)P_2$ and 16.7 nm for membranes containing $PI(4,5)P_2$, were smaller than their bare counterparts, 32.9 nm for membranes containing $PI(3,4)P_2$ and 35.5 nm for membranes containing $PI(4,5)P_2$ (Fig 4C). This difference in mean diameters indicates the capacity of SNX9 to deform membranes and to constrict tubes down to approximately 15 nm in diameter, consistent with spontaneous membrane curvature observed in our tube pulling experiments (Fig. 4). For both $PIP_2$ conditions, we also observed peanut-shaped vesicles characterized by a neck-like structure at the center. At these necks, the membranes appear less defined and fuzzier as compared to the rest of the membranes on the vesicles, indicating SNX9 enrichment at these necks, showing again the membrane shaping effect of SNX9 (Fig. 4). In summary, for both $PI(4,5)P_2$ and PI(3,4)P2-containing membranes SNX9 exhibits a loose organization on tubular membrane geometries, and preferentially binds to curved, tubular membranes. This binding in turns induces substantial membrane deformations, transforming vesicles into peanut shapes with pinched necks, and eventually into thin tubes.

### SNX9 PX-BAR Drives Distinct Distributions of $PI(3,4)P_2$ and $PI(4,5)P_2$ Lipids

To explore the molecular mechanisms by which SNX9 interacts with membranes containing $PI(4,5)P_2$ and $PI(3,4)P_2$, we conducted all-atom molecular dynamics (AA-MD) simulations of the dimeric SNX9 PX-BAR domains (residues 200-595) with model membranes containing the following compositions: DOPC:DOPS 80:20; DOPC:DOPS:$PI(3,4)P_2$ 80:15:5; and DOPC:DOPS:$PI(4,5)P_2$ 80:15:5 (Fig. 5A). By probing the unbiased interactions between SNX9-PXBAR and model membranes, we aimed to understand whether there is a difference in the way that SNX9 interacts with $PI(3,4)P_2$ and $PI(4,5)P_2$. Specifically, we sought to investigate how SNX9 PX-BAR influences the local dynamics of $PIP_2$ lipids upon binding.

Although the timescales achievable by AA-MD (a total of 5 microseconds for each composition) limits direct measurement of kinetic rate constants, the simulations enable detailed analysis of nanoscopic phenomena such as lipid diffusion. To this end, we calculated the total distance traversed by all lipids and visualized the trajectory traces over time, using threshold distances as a color-coded guide (Fig. 5, C-F, Supplementary Figures 1-4). These trace analyses demonstrate that SNX9 PX-BAR sequesters multiple $PIP_2$ lipids in its immediate vicinity.

The sequestration effect of $PIP_2$ is most pronounced at the time-averaged positions of the PX domains and the center of the BAR domain (CBD) (Supplementary Figures 1-4, with SNX9-PXBAR overlay). These findings indicate that these regions are most strongly implicated in $PIP_2$ binding. While the PX domain has been previously identified as the primary site of $PIP_2$ binding, the CBD binding has not been reported in lipid binding. Notably, previous mutational assays have implicated the CBD region in autoinhibition of SNX9, but no lipid selectivity has been reported(*34*). Structural predictions of SNX9 linker region implicated in autoinhibition position the linker region near the CBD. This alignment suggests that the positively charged CBD may mediate nonspecific interactions with $PIP_2$ (Supplementary Figure 5). Given the plausible non-specific CBD-lipid binding, we focused on the PX domain to investigate the mechanism underlying SNX9's selectivity for $PI(3,4)P_2$ and $PI(4,5)P_2$.

We observed that in the upper leaflet of the membranes where SNX9 PX-BAR is bound, there is super-stoichiometric sequestration of $PIP_2$ lipids (Fig. 5 B,C). The averaged binding ratios per PX domain with standard deviation are 3.3±0.6 for $PI(3,4)P_2$ and 3.±1. for $PI(4,5)P_2$ (Supplementary Table 1). These binding ratios, exceeding a value of unity, challenge the canonical lock-and-key interaction paradigm that assumes a single $PIP_2$ lipid fits into a tight binding pocket. Instead, they suggest that the SNX9 PX domain can engage multiple lipids simultaneously through a multivalent binding mechanism. Supporting this, we find that almost all of the PX domains in our simulations showed a binding occupancy of at least two lipids. The similarity in average binding ratios between $PI(3,4)P_2$ and $PI(4,5)P_2$ can be attributed to this multivalency, as having multiple binding subdomains that simultaneously bind to the membrane will be the greatest influence on average interactions.

To determine whether the observed superstoichiometric binding is due to specific SNX9 PX-BAR and $PIP_2$ interactions rather than the intrinsic properties of the $PIP_2$ lipids we analyzed the average dynamics of the lipids. As shown in Fig. 5D, we observe significant differences in the distance traveled by the $PIP_2$ lipids near the SNX9 PX-BAR domain compared to unbound $PIP_2$ lipids in the upper leaflet and those in the lower leaflet (Supplementary Figure 6). We note that there is no significant difference in the total distance traveled between unbound $PIP_2$ lipids in the upper leaflet and in the lower leaflet (Supplementary Figure 6). Additionally, no significant spatial variation of $PIP_2$ lipids in lower leaflet was observed, which indicates the absence of trans-bilayer coupling due to SNX9 PX-BAR binding. Comparing between $PI(3,4)P_2$ and $PI(4,5)P_2$ in the lower leaflet, there is no significant difference in the radius of gyration, a measure of lipid motion, indicating that the dynamics of the individual $PIP_2$ lipids are similar on average. Furthermore, there is a similar correspondence in the radius of gyration values of DOPS and DOPC lipids across all the membrane conditions simulated, indicating that there is no difference in the local effects of $PIP_2$ lipids on the neighboring lipids; put another way, the presence of PIP2 does not locally change the dynamics of other lipids (Supplementary Figure 7). Additionally, we quantified the average network connectivity of

$PIP_2$ clustering as measure of average cluster size and found no significant differences either between the bilayers containing $PI(3,4)P_2$ versus $PI(4,5)P_2$ nor between the upper (SNX9 bound) and lower (no protein bound) leaflets of each bilayer (Supplementary Figure 8). The lack of observable clustering among $PIP_2$ is consistent with previous findings, given the ionic composition of our simulations and the local sequestration effect observed(*35*). Taken together, our results indicate that the observed lipid selective sequestration is not driven by intrinsic differences in $PI(3,4)P_2$ and $PI(4,5)P_2$ behaviors. Instead, the specificity arises from direct interactions between SNX9 PX-BAR and $PIP_2$ lipids, particularly those mediated by the PX domain.

To further exclude explanations of the local sequestration based on membrane-mediated effects, we explored possible changes in the behaviors of DOPC and DOPS, as well as changes in overall membrane properties. We found no significant difference in the average radius of gyration and the spatial distributions of DOPC or DOPS in membranes containing or lacking $PIP_2$ lipids (Supplementary Figure 7 and 9). Global membrane properties such as mean curvature and membrane packing defects also showed no significant differences between the three membrane compositions tested in the presence of SNX9 (Supplementary Figures 10, 11). These results indicate that neither the behavior of lipid species present in the membrane nor of the global membrane properties are altered in ways that could explain the observed $PI(3,4)P_2$ selectively sequestering by the PX domain of SNX9.

## The SNX9-PX Membrane Binding Interface is Larger Than Previously Identified

We next sought to identify PX-$PIP_2$ contacts to determine whether previously characterized canonical binding residues are responsible for $PIP_2$ selectivity. By analyzing the frequency of direct contacts between residues in the PX domain and the central phosphorus of $PI(3,4)P_2$ and $PI(4,5)P_2$, we identified three distinct subdomains interacting with $PIP_2$ (Fig. 6). These subdomains are referred to as the insert loop, the canonical pocket, and the fourth helix. We note that the identification of these three subdomains aligns well with the average binding ratios of 3.6 and 3.4 for $PI(3,4)P_2$ and $PI(4,5)P_2$, respectively, indicating that one or more of these subdomains can interact with multiple $PIP_2$ lipids. These subdomains are broad, ranging from 11 to 19 residues with strong membrane interactions, and extend beyond the canonical residues previously identified through sequence alignment(*8*). Between the large membrane interface and observed superstoichiometric binding, the question of selectivity mechanisms should be addressed within each of the subdomains.

The insert loop subdomain (residues 258-270) is rich in lysines and hydrophobic residues. Its conserved motif, x**K**x(S/T)**KΦ**xG**ΦKSYI** (where x represents non-conserved residues, and Φ represents a large hydrophobic residue), is shared by SNX9 and closely related members of the SNX family, SNX18 and SNX33 (Supplementary Figure 12). The flexibility and composition of this subdomain allows it to penetrate the membrane and interact with negatively charged lipids, anchoring the PX domain to the membrane. It is therefore not surprising that the insert loop shows the highest frequency of contacts with the central phosphate group of both $PI(3,4)P_2$ and $PI(4,5)P_2$. Unlike the canonical pocket and fourth helix subdomains where their PIP2 interactions relies on specific residues, the PIP2 interactions of the insert loop is broadly across its entire length, reflecting its critical role in PIP2 interactions (Fig. 6)

The canonical pocket subdomain (residues 286-293 and 309-320) has been the primary focus in studying $PIP_2$ selectivity and binding. Crystal structures of SNX9 PX-BAR domain, along with analogous structural studies of other PX domains, have suggested that the PIP headgroup resides within this pocket, stabilized by a conserved set of residues (*8, 11*). However, while the canonical pocket of SNX9 does interface with the $PIP_2$ lipids in the membrane, we observed that the conserved residues Tyr294, Arg296, and Lys300 do not interact with the membrane at all (designated with pink * in Fig. 6). Furthermore, compared to the insert loop, the canonical pocket exhibits greater variation in contact frequency with $PIP_2$ among the sequential residues in the loop, due to its more rigid tertiary structure.

The fourth helix subdomain (residues 358-370), which is not traditionally considered as part of the PX domain, lies adjacent to the BAR domain and interacts frequently with the membrane (Fig. 6). Like the canonical pocket, this forth helix subdomain exhibits variation in PIP2 contact frequency among sequential residues due to its rigid secondary and tertiary structure. While the net charge of the fourth helix is +2, its four positively charged residues (Lys363, Lys367, Arg368, and Arg370) are aligned along its membrane-facing surface. This alignment strongly favor binding to negatively charged lipids such as the PIPs and PS. The alignment of these positively charged residues along the membrane binding surface of the fourth helix suggests that its protruding sidechains could synergistically coordinate the large headgroup of a $PIP_2$ lipid.

**The SNX9-PX Fourth Helix Promotes PI(3,4)$P_2$ Selectivity**

Of the three subdomains identified in this study, only the canonical pocket and the fourth helix interact with $PIP_2$ primarily through electrostatic interactions, specifically involving positively charged residues. Because $PIP_2$ lipids are strongly negatively charged, - 4 compared to -1 for PI and PS at physiological pH, and have a bulky phosphoinositide headgroup, the specific arrangements of positively charged residues in the canonical pocket and fourth helix are likely key for explaining how the SNX9 PX domain selectively interacts with PI(3,4)$P_2$ over PI(4,5)$P_2$. The electrostatic map of the membrane binding face of SNX9 PX domain clearly shows the importance of these positively charged residues (Fig. 7A). It also highlights the formation of two distinct pockets of charge surrounding the canonical pocket and the fourth helix.

To investigate how these residues could cooperatively bind to the same $PIP_2$ lipid, we calculated a contact frequency for all positively charged residues based on the Bjerrum length, considering instances when two residues coordinate the same lipid, though not necessarily the same phosphate group (Fig. 7B, Supplementary Figure 13)(*19*). This cooperative frequency based on electrostatic binding groups provides deeper insight into the specificity of lipid interactions. By identifying residues with cooperative self-contact frequencies greater than 1.5, we can determine those involved in major coordination events (Fig. 7C). For the canonical pocket, the major coordinating residues were identical for both PI(3,4)$P_2$ and PI(4,5)$P_2$, and include Arg286, Lys288, Lys313, and Arg318. However, for the fourth helix, we find a broader set of coordinating residues for PI(3,4)$P_2$ over PI(4,5)$P_2$. Specifically, residues Lys360, Lys363, Lys366, Arg,367, Lys368 and Arg371 for PI(3,4)$P_2$, and Lys363, Lys366, Arg367 and Arg371 for PI(4,5)$P_2$, indicating stronger coordinating interactions for PI(3,4)$P_2$ (Fig. 7). Besides, we observe a stronger interaction network between all the residues in the fourth helix for PI(3,4)$P_2$

over PI(4,5)$P_2$ (Fig. 7E). This reinforces the idea of a more robust coordination for PI(3,4)$P_2$, and provides an explanation for how selectivity is maintained, despite superstoichiometric binding ratios. The expansive network of coordinating residues is capable of binding multiple $PIP_2$ lipids simultaneously. Furthermore, inter-domain contacts, particularly between the fourth helix and the canonical pocket subdomains, are stronger for PI(3,4)$P_2$ than for PI(4,5)$P_2$ (Supplementary Figure 14). In addition to electrostatic differences, we note that the canonical pocket has a significantly smaller cavity volume of 745 $Å^3$ compared to the volume of the fourth helix subdomain of 905 $Å^3$ (Supplementary Figure 14). Docking predictions further suggest that both PI(3,4)$P_2$ and PI(4,5)$P_2$ are most likely to bind to the fourth helix subdomain than the canonical pocket (Supplementary Figure 14). Collectively, our findings indicate that SNX9 PX domain has a selectivity for PI(3,4)$P_2$ over PI(4,5)$P_2$, through the fourth helix of the PX domain.

### SNX9 Prevents the Hydrolysis of PI(3,4)$P_2$ by INPP4B

Based on our simulation results showing that SNX9 PX-BAR dimers sequester PI(3,4)$P_2$, we hypothesized that SNX9 may influence the hydrolysis of PI(3,4)$P_2$ by INPP4B phosphatase. This hydrolysis is critical in macropinocytosis, converting PI(3,4)$P_2$ to PI(3)P for macropinosome closure. By monitoring PI(3,4)$P_2$ enrichment at the plasma membrane of cells overexpressed membrane-bound INPP4B (INPP4B-CAAX), we assess whether SNX9 protects PI(3,4)$P_2$ from INPP4B-mediated hydrolysis through sequestration. Consistent with previous reports, overexpression of wild-type INPP4B (INPP4B-WT), but not the catalytic dead C842S mutant (INPP4B-CS), significantly reduces PI(3,4)$P_2$ enrichment at plasma membrane ruffles (Fig. 8A, B)(*36*). Intriguingly, overexpression of SNX9-mScarlet restores PI(3,4)$P_2$ at the plasma membrane of cells expressing INPP4B-WT (Fig. 8A). This result highlights SNX9's protective role in shielding PI(3,4)$P_2$ from hydrolysis by INPP4B.

To reveal the functional relevance of SNX9's PX interaction networks in coordinating PI(3,4)$P_2$ that our simulations identified, we performed specific mutations in the SNX9-PX domain, and assessed the consequences of PI(3,4)$P_2$ conversion in cellular assays with either functional or non-functional INPP4B phosphatase (Fig. 8B). We found that loss-of-function mutations in SNX9, K313A in the canonical pocket and K366/367A in the fourth helix, fail to rescue PI(3,4)$P_2$ enrichment in cells expressing INPP4B-WT, despite their proper localization at the plasma membrane (Fig. 8C-D). Conversely, gain-of-function mutations in SNX9, K366R and K366/368R both in the fourth helix, more effectively restored PI(3,4)$P_2$ enrichment the plasma membrane. These mutants recapitulated the protective capacity of wide-type SNX9 INPP4B-meidated hydrolysis (Fig 8). Notably, in cells expressing the non-functional phosphatase, INPP4B C842A, PI(3,4)$P_2$ enrichment index is comparable among all SNX9 variants, indicating that the observed effects of SNX9 on PI(3,4)$P_2$ coordination are specific to the functional interaction with INPP4B (Fig. 8E).

## DISCUSSION

We have presented evidence that PI(3,4)$P_2$ and PI(4,5)$P_2$ exhibit distinct spatial distributions upon interacting with SNX9 PX-BAR domain. While both PI(3,4)$P_2$ and PI(4,5)$P_2$ bind superstoichiometrically to SNX9 via the membrane-remodeling PX-BAR domain, we

identified the non-canonical Helix 4 interface in the PX domain as a significant differential contributor to how $PIP_2$ lipids are localized, providing mechanistic insight into how lipid selectivity can co-exist with the high valency of peripheral membrane protein binding. While the magnitude of the effect is modest, it translates *in vivo* to the tight spatiotemporal colocalization of SNX9 with $PI(3,4)P_2$ over $PI(4,5)P_2$ at macropinocytic ruffles. Due to the generality of the biophysics at play, this selective binding is thus likely to be a strongly influencing factor in the spatiotemporal recruitment of peripheral membrane proteins to not only the plasma membrane during macropinocytosis, as in the case of SNX9, but broadly apply for many proteins containing lipid selective domains including PX, PH, FYVE, and C2.

The Helix 4 interface, identified as driving selectivity of SNX9 for $PI(3,4)P_2$ over $PI(4,5)P_2$, provides the opportunity to reflect more broadly on our treatment of peripheral membrane protein binding modes. We have endeavored to emphasize here that even for traditionally lipid selective domains such as the PX domain, multiple lipids are simultaneously bound and so determining selectivity is not always a straightforward task, and requires a detailed look at the structure and dynamics of the domain of interest on a membrane. Sequence data is helpful for identifying conserved residues that may play an important role, but should be paired whenever possible with structural analysis to ensure that the identified residues are part of the binding interface of interest.

To determine the mechanism of SNX9 Helix 4 selectivity for $PI(3,4)P_2$ over $PI(4,5)P_2$, we demonstrated the importance of a non-canonical binding interface with a network of positively charged residues that coordinate the $PIP_2$ headgroup (Fig. 7). The large, negatively charged headgroup of the $PIP_2$ lipids define their interactions with peripheral membrane proteins, and distinguishes them particularly from other lipid classes; therefore, the electrostatic interaction mechanism proposed, coupled with spatial understanding of the non-canonical binding interface (i.e., how the positively charged sidechains face the membrane (Fig. 7) and the larger cavity size of the non-canonical interface (Supplementary Figure 14)), is grounded by physical arguments and supported by the mutational assays (Fig. 8). While we primarily probed the electrostatic impact by mutating positively charged residues, further work could probe the effect of interface size by introducing bulky, neutral sidechains that would protrude into the adjoining cavity. However, the introduction of such residues could disrupt the protein tertiary structure or lead to insertion of these large neutral residues into the membrane, significantly altering the membrane binding mode as opposed to only probing $PIP_2$ selectivity.

The slight magnitude of this selectivity can also be partially attributed to the non-specific superstoichiometric binding of SNX9 PXBAR to the membrane. Multiple lipids binding simultaneously in non-specific ways can make it difficult to determine the impact of a single lipid specifically binding, which may explain why previous *in vitro* literature has reported seemingly contradictory results and weak binding for the SNX9 PX domain, particularly in isolation from the BAR construct. Superstoichiometric binding is likely a general strategy to recruit peripheral membrane binding proteins to the membrane surface, while specific binding may play a role in retention there. The observed general reduction of lipid mobility around the SNX9-PXBAR domain due to this superstoichiometric binding may be part of the mechanism of protein-mediated $PIP_2$ aggregation, which has been previously reported for inverse BAR proteins(*37, 38*). However, aggregation is a collective effect, and therefore further *in silico* studies should include a much larger membrane system with at least dozens of PX-BAR domains to investigate this phenomenon.

Using reconstituted assays, we have demonstrated that SNX9 possesses both membrane curvature sensing and remodeling capabilities of SNX9, regardless of PIP types. While many BAR domains have been characterized as curvature sensing and generating, our study provides a quantitative analysis of the curvature sensing capability of full-length SNX9. We found that SNX9-enriched membrane tubes exhibit diameters comparable to those of membrane necks in clathrin-mediated endocytosis, and with cryo-EM imaging of dynamin tubes (*29, 39*). These findings support SNX9's mechanistic role in shaping the membrane neck during lipid conversion in endocytosis. Additionally, Cryo-EM experiments reveal an irregular organization of SXN9 on membrane tubes, suggesting that SNX9 remains bound throughout endocytosis, facilitating the recruitment of downstream partners ush as dynamin and N-WASP.

Putting it all together, we hypothesize and demonstrate a role for SNX9, and the Helix 4 interface of SNX9-PX, in macropinocytosis beyond curvature generation or downstream protein recruitment – as a checkpoint to prevent the premature hydrolysis of PI(3,4)$P_2$ to PI(3)P by INPP4B. This is an important and overlooked role in membrane remodeling processes that include lipid compositional changes (as most do); the timescale of enzymatic lipid conversion is fast compared to micron-scale remodeling, and the regulated coordination of these processes is critical for ensuring successful internalization. Therefore, SNX9 having two distinct membrane binding domains, the BAR and PX domains, allows it to simultaneously sense and effect 'global' properties of the plasma membrane (i.e. curvature, via the BAR domain), while also sensing *and* regulating 'local' compositional properties (i.e. PI(3,4)$P_2$ concentration, via the PX domain). This functional cooperativity between domains has been shown for PXBAR-domain containing protein SNX1, and is likely a generalizable effect(*40*). While not the focus of this study, the previously observed hetero-dimerization of SNX9 with SNX18 could offer a further expanded repertoire of capabilities, and offers a suggestive hint of why there may be so many distinct BAR domain containing proteins(*41*). We note that this does not imply that composition is the exclusive mechanism of recruitment, as other membrane properties such as curvature also change significantly during membrane remodeling events and thus drive protein recruitment. Given our results suggesting that SNX9 responds similarly to membranes of similar curvature containing either PI(3,4)$P_2$ or PI(4,5)$P_2$ (Fig. 2, Supplementary Figure 11), we suggest that curvature may be secondary to selectivity for SNX9 recruitment. SNX9, in turn, recruits other downstream protein partners via its SH3 domain, thus providing a mechanism by which PI(3,4)$P_2$ lipids indirectly coordinate ruffle maturation.

Once SNX9 binds to the plasma membrane upon appearance of PI(3,4)$P_2$, it appears to provide a "protective" capacity preventing the conversion of PI(3,4)$P_2$ to PI(3)P. Given the importance of membrane composition in coordinating membrane remodeling, this effect is particularly critical and likely acts as a checkpoint to ensure that the remodeling process has sufficiently matured before proceeding. While it is not clear from this work exactly what signal eventually drives SNX9 to dissociate from the membrane and free PI(3,4)$P_2$ for conversion by INPP4B and other phosphatases, the changes in Gaussian membrane curvature as a result of scission could be an important signal to induce a mechanical change in SNX9 organization from a loosely organized but deeply interacting scaffold on tubes to more shallow contacts on spherical vesicles, as has been demonstrated for other BAR domain containing proteins(*42, 43*).

It is striking to note how lipid selectivity between two nearly identical lipids, PI(3,4)$P_2$ and PI(4,5)$P_2$, arises from simple effects such as electrostatics and spatial arrangements despite the

high valency of peripheral membrane proteins, and further how selectivity drives the coordination of complex remodeling processes at the plasma membrane. We anticipate that these conclusions are not unique to SNX9 nor the plasma membrane, but rather provide insights into the biophysics behind selective membrane recruitment for a host of peripheral membrane proteins.

Works Cited


1. N. Araki, Y. Egami, Y. Watanabe, T. Hatae, Phosphoinositide metabolism during membrane ruffling and macropinosome formation in EGF-stimulated A431 cells. *Exp Cell Res* **313**, 1496-1507 (2007).
2. M. Maekawa *et al.*, Sequential breakdown of 3-phosphorylated phosphoinositides is essential for the completion of macropinocytosis. *Proc Natl Acad Sci USA* **111**, E978-987 (2014).
3. D. J. Gillooly, C. Raiborg, H. Stenmark, Phosphatidylinositol 3-phosphate is found in microdomains of early endosomes. *Histochem Cell Biol* **120**, 445-453 (2003).
4. G. Di Paolo, P. De Camilli, Phosphoinositides in cell regulation and membrane dynamics. *Nature* **443**, 651-657 (2006).
5. Y. Posor, W. Jang, V. Haucke, Phosphoinositides as membrane organizers. *Nat Rev Mol Cell Biol* **23**, 797-816 (2022).
6. J. Ray, D. G. Sapp, G. D. Fairn, Phosphatidylinositol 3,4-bisphosphate: Out of the shadows and into the spotlight. *Curr Opin Cell Biol* **88**, 102372 (2024).
7. M. Overduin, T. A. Kervin, The phosphoinositide code is read by a plethora of protein domains. *Expert Rev Proteomics* **18**, 483-502 (2021).
8. M. Chandra *et al.*, Classification of the human phox homology (PX) domains based on their phosphoinositide binding specificities. *Nat Commun* **10**, 1528 (2019).
9. E. E. Kooijman, A. Gericke, Physical chemistry and biophysics of polyphosphoinositide mediated lipid signaling. *Chem Phys Lipids* **182**, 1-2 (2014).
10. E. E. Kooijman, K. E. King, M. Gangoda, A. Gericke, Ionization properties of phosphatidylinositol polyphosphates in mixed model membranes. *Biochemistry* **48**, 9360-9371 (2009).
11. O. Pylypenko, R. Lundmark, E. Rasmuson, S. R. Carlsson, A. Rak, The PX-BAR membrane-remodeling unit of sorting nexin 9. *EMBO J* **26**, 4788-4800 (2007).
12. D. F. J. Ceccarelli *et al.*, Non-canonical interaction of phosphoinositides with pleckstrin homology domains of Tiam1 and ArhGAP9. *J Biol Chem* **282**, 13864-13874 (2007).
13. T. Xu *et al.*, Molecular basis for PI(3,5)P2 recognition by SNX11, a protein involved in lysosomal degradation and endosome homeostasis regulation. *J Mol Biol* **432**, 4750-4761 (2020).
14. C.-Z. Zhou *et al.*, Crystal structure of the yeast Phox homology (PX) domain protein Grd19p complexed to phosphatidylinositol-3-phosphate. *J Biol Chem* **278**, 50371-50376 (2003).
15. D. Kerr, T. Suwatthee, S. Maltseva, K. Y. C. Lee, Binding equations for the lipid composition dependence of peripheral membrane-binding proteins. *Biophys J* **123**, 885-900 (2024).
16. K. Moravcevic, C. L. Oxley, M. A. Lemmon, Conditional peripheral membrane proteins: facing up to limited specificity. *Structure* **20**, 15-27 (2012).
17. M. A. Lemmon, Membrane recognition by phospholipid-binding domains. *Nat Rev Mol Cell Biol* **9**, 99-111 (2008).
18. J. J. Falke, B. P. Ziemba, Interplay between phosphoinositide lipids and calcium signals at the leading edge of chemotaxing ameboid cells. *Chem Phys Lipids* **182**, 73-79 (2014).
19. T. Ehret *et al.*, FERM domains recruit ample PI(4,5)P2s to form extensive protein-membrane attachments. *Biophys J* **122**, 1325-1333 (2023).
20. E. Yamamoto *et al.*, Multiple lipid binding sites determine the affinity of PH domains for phosphoinositide-containing membranes. *Sci Adv* **6**, eaay5736 (2020).
21. E. Yamamoto, A. C. Kalli, K. Yasuoka, M. S. P. Sansom, Interactions of Pleckstrin Homology Domains with Membranes: Adding Back the Bilayer via High-Throughput Molecular Dynamics. *Structure* **24**, 1421-1431 (2016).
22. T. Sasaki *et al.*, Mammalian phosphoinositide kinases and phosphatases. *Prog Lipid Res* **48**, 307-343 (2009).
23. N. Singh *et al.*, Redefining the specificity of phosphoinositide-binding by human PH domain-containing proteins. *Nat Commun* **12**, 4339 (2021).
24. M. Simunovic, E. Evergren, A. Callan-Jones, P. Bassereau, Curving cells inside and out: roles of BAR domain proteins in membrane shaping and its cellular implications. *Annu Rev Cell Dev Biol* **35**, 111-129 (2019).
25. F. Soulet, D. Yarar, M. Leonard, S. L. Schmid, SNX9 regulates dynamin assembly and is required for efficient clathrin-mediated endocytosis. *Mol Biol Cell* **16**, 2058-2067 (2005).
26. N. Shin *et al.*, Sorting nexin 9 interacts with dynamin 1 and N-WASP and coordinates synaptic vesicle endocytosis. *J Biol Chem* **282**, 28939-28950 (2007).
27. F. Daste *et al.*, Control of actin polymerization via the coincidence of phosphoinositides and high membrane curvature. *J Cell Biol* **216**, 3745-3765 (2017).

28. J. L. Gallop, A. Walrant, L. C. Cantley, M. W. Kirschner, Phosphoinositides and membrane curvature switch the mode of actin polymerization via selective recruitment of toca-1 and Snx9. *Proc Natl Acad Sci USA* **110**, 7193-7198 (2013).
29. J. Schöneberg *et al.*, Lipid-mediated PX-BAR domain recruitment couples local membrane constriction to endocytic vesicle fission. *Nat Commun* **8**, 15873 (2017).
30. D. Yarar, C. M. Waterman-Storer, S. L. Schmid, SNX9 couples actin assembly to phosphoinositide signals and is required for membrane remodeling during endocytosis. *Dev Cell* **13**, 43-56 (2007).
31. Y. Posor *et al.*, Spatiotemporal control of endocytosis by phosphatidylinositol-3,4-bisphosphate. *Nature* **499**, 233-237 (2013).
32. B. Sorre *et al.*, Nature of curvature coupling of amphiphysin with membranes depends on its bound density. *Proc Natl Acad Sci USA* **109**, 173-178 (2012).
33. C. Mim *et al.*, Structural basis of membrane bending by the N-BAR protein endophilin. *Cell* **149**, 137-145 (2012).
34. W.-T. Lo *et al.*, A Coincidence Detection Mechanism Controls PX-BAR Domain-Mediated Endocytic Membrane Remodeling via an Allosteric Structural Switch. *Dev Cell* **43**, 522-529.e524 (2017).
35. K. Han, A. Gericke, R. W. Pastor, Characterization of Specific Ion Effects on PI(4,5)P2 Clustering: Molecular Dynamics Simulations and Graph-Theoretic Analysis. *J Phys Chem B* **124**, 1183-1196 (2020).
36. C. Gewinner *et al.*, Evidence that inositol polyphosphate 4-phosphatase type II is a tumor suppressor that inhibits PI3K signaling. *Cancer Cell* **16**, 115-125 (2009).
37. F.-C. Tsai *et al.*, Activated I-BAR IRSp53 clustering controls the formation of VASP-actin-based membrane protrusions. *Sci Adv* **8**, eabp8677 (2022).
38. Z. Jarin, A. J. Pak, P. Bassereau, G. A. Voth, Lipid-Composition-Mediated Forces Can Stabilize Tubular Assemblies of I-BAR Proteins. *Biophys J* **120**, 46-54 (2021).
39. J. Liu, F. J. D. Alvarez, D. K. Clare, J. K. Noel, P. Zhang, CryoEM structure of the super-constricted two-start dynamin 1 filament. *Nat Commun* **12**, 5393 (2021).
40. Z. Liao, T. Si, J.-J. Kai, J. Fan, Mechanism of Membrane Curvature Induced by SNX1: Insights from Molecular Dynamics Simulations. *J Phys Chem B* **128**, 2144-2153 (2024).
41. J. Park *et al.*, SNX18 shares a redundant role with SNX9 and modulates endocytic trafficking at the plasma membrane. *J Cell Sci* **123**, 1742-1750 (2010).
42. E. Boucrot *et al.*, Membrane fission is promoted by insertion of amphipathic helices and is restricted by crescent BAR domains. *Cell* **149**, 124-136 (2012).
43. J. M. Isas, M. R. Ambroso, P. B. Hegde, J. Langen, R. Langen, Tubulation by amphiphysin requires concentration-dependent switching from wedging to scaffolding. *Structure* **23**, 873-881 (2015).

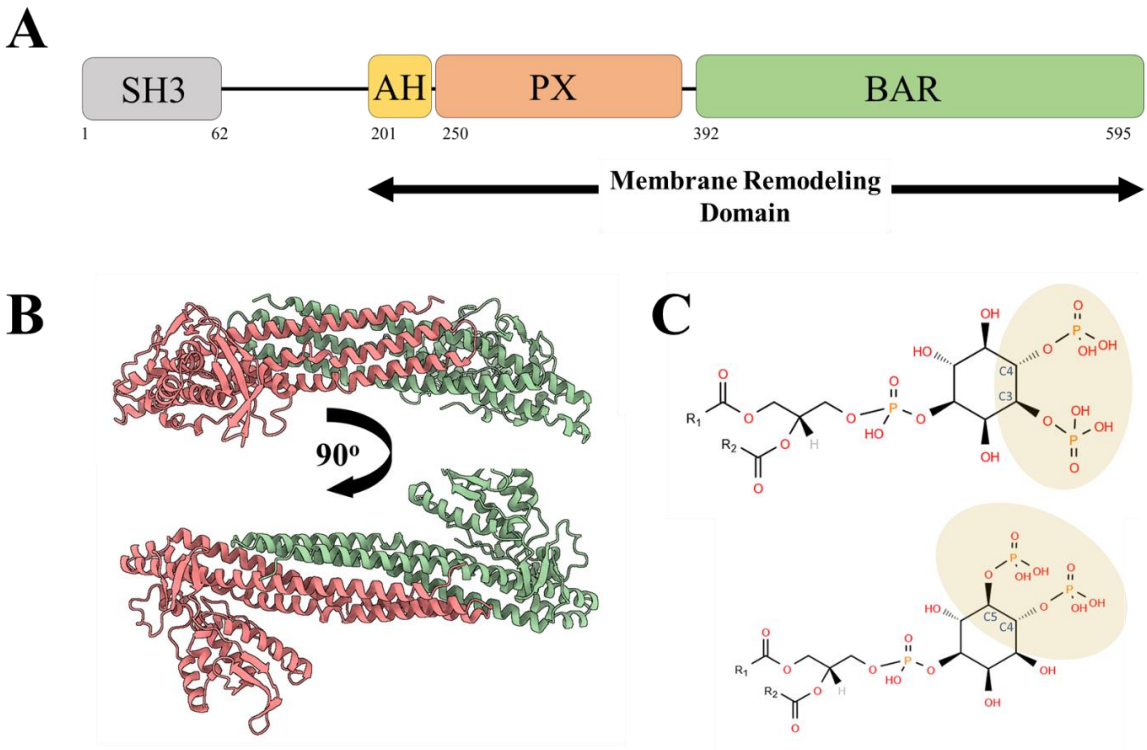


**Figure 1. Structural information about sorting nexin 9 (SNX9), PI(3,4)$P_2$, and PI(4,5)$P_2$. (A)** Schematic of domains of SNX9, in sequence order. The range from residues 200-595 is collectively known as the membrane remodeling domain. SH3 – SRC Homology 3; AH – amphipathic helix; PX – Phox homology; BAR – Bin/Amphiphysin/Rvs domain. **(B)** Predicted structure of the membrane remodeling domain of SNX9 dimer viewed from the side (top) and looking top-down (bottom); the predicted structure has an RMSD from that of the apo crystal structure of 1.196 Å (PDB ID: 2RAI) and of the PI(3)P bound crystal structure of 1.271 Å (PDB ID: 2RAK). **(C)** Stereoprojected line structures of the headgroups of PI(3,4)$P_2$ (top) and PI(4,5)$P_2$ (bottom), with the C3 and C4 or C4 and C5 inositol carbons (respectively) labelled to demonstrate the location of the phosphate functional groups. Line structures obtained from LIPID MAPS® structure database.

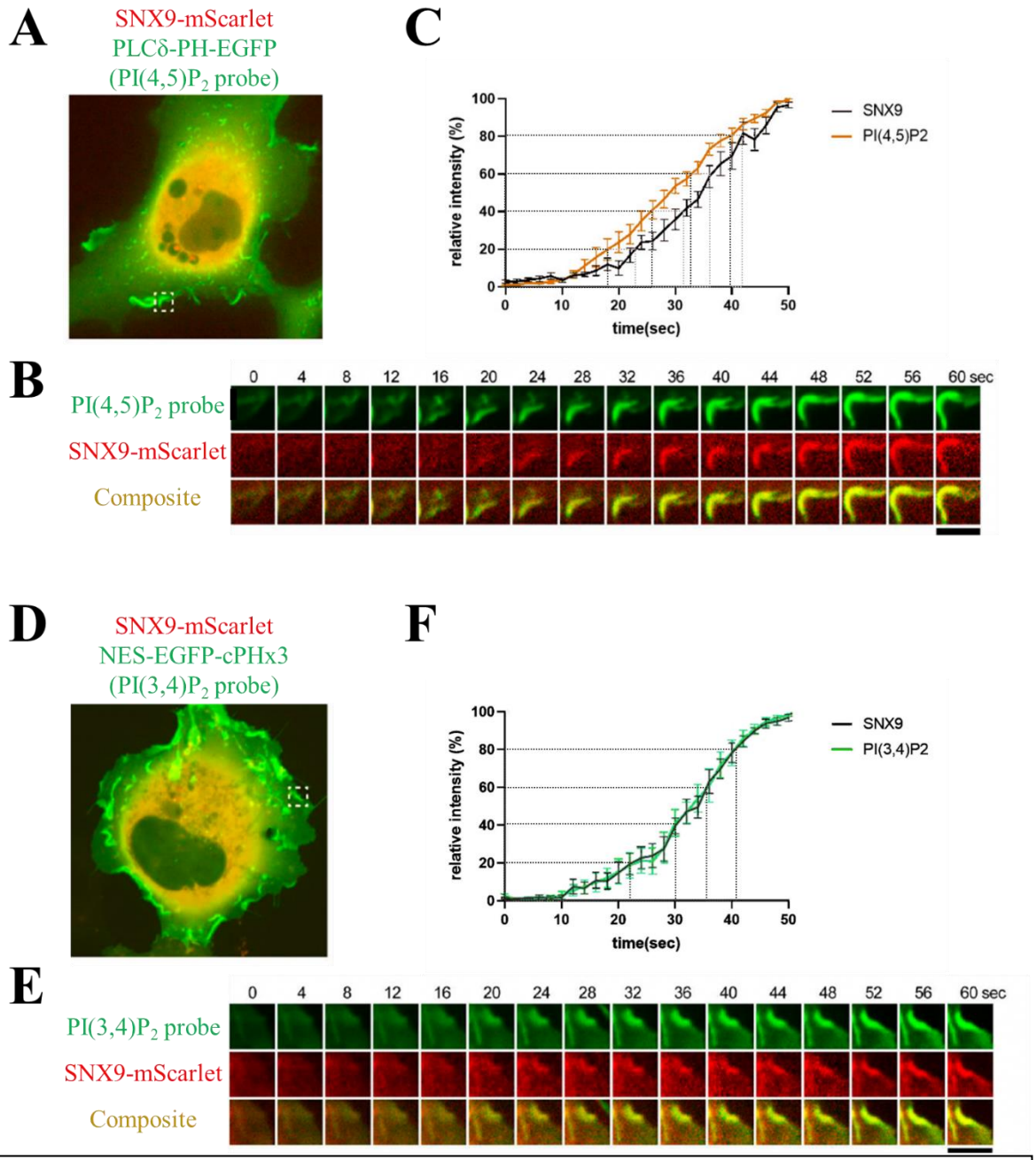


**Figure 2:** SNX9 recruitment to macropinocytic ruffles lags PI(4,5)$P_2$ appearance and is coincident with PI(3,4)$P_2$ appearance. **(A)** Representative overlay image of SNX9 (red) and PI(4,5)$P_2$ (green) fluorescent probe signals. The white inset box highlights the ruffle shown in (B). **(B)** Time series evolution of the signal of PI(4,5)$P_2$ (green) and SNX9 (red) from a macropinocytic ruffle over the first 60 seconds of ruffle formation. Scale bar is 5 µm. **(C)** Plot of relative intensity of fluorescent signal for PI(4,5)$P_2$ and SNX9 from time series, quantified over 12 ruffles. Guidelines show the time of 20%, 40%, 60%, and 80% relative intensity for both the SNX9 and PI(4,5)$P_2$ signals. **(D)** Representative overlay image of SNX9 (red) and PI(3,4)$P_2$ (green) fluorescent probe signals. The white inset box highlights the ruffle shown in (E). **(E)** Time series evolution of the signal of PI(3,4)$P_2$ (green) and SNX9 (red) from a macropinocytic ruffle over the first 60 seconds of ruffle formation. Scale bar is 5 µm. **(F)** Plot of relative intensity of fluorescent signal for PI(3,4)$P_2$ and SNX9 from time series, quantified over 11 ruffles. Guidelines show the time of 20%, 40%, 60%, and 80% relative intensity for both the SNX9 and PI(3,4)$P_2$ signals.

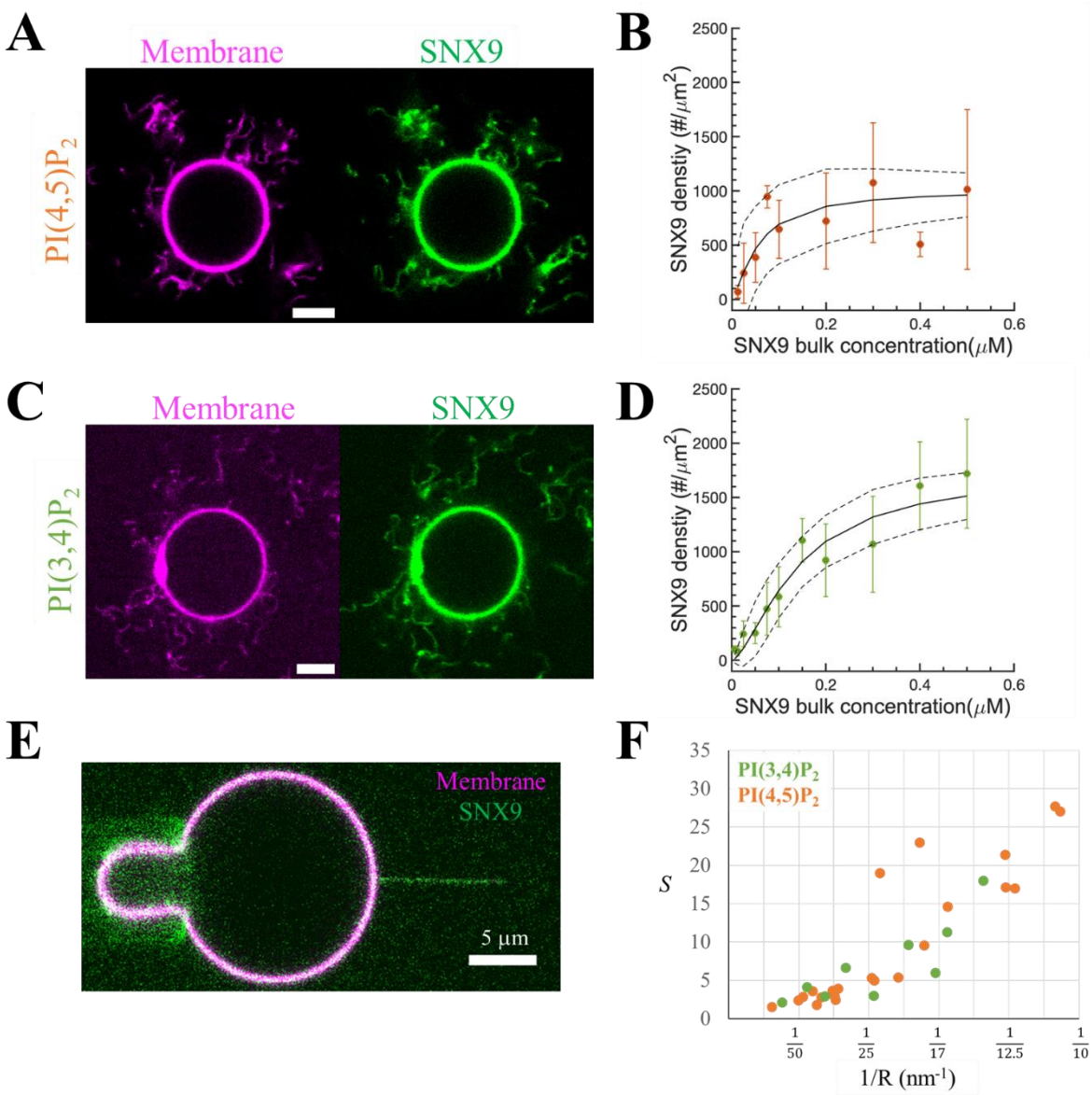


**Figure 3.** SXN9 generates membrane tubes and binds with comparable affinities on PI(3,4)P2 and PI(4,5)P2-GUVs. **(A)** GUVs exhibiting outward tubes generated by SNX9 on membranes containing PI(4,5)$P_2$. **(B)** Analysis of SNX9's binding on GUVs containing PI(4,5)$P_2$. **(C)** GUVs exhibiting outward tubes generated by SNX9 on membranes containing PI(3,4)$P_2$. **(D)** Analysis of SNX9's binding on GUVs containing PI(3,4)$P_2$. Surface densities of SNX9, $\phi_v$, determined for (B) and (D) from the fluorescence signals, as a function of SNX9 bulk concentration $C_{bulk}$. The data were fitted to $\phi_v = \frac{\phi_{max} \times {C_{bulk}}^n}{K_d + {C_{bulk}}^n}$, where $\phi_{max}$ is the maximum surface density, $K_d$ is the dissociation constant and $n$ is the Hill coefficient. We obtained $K_d = 31\ nM$ and n=1.18 for PI(4,5)$P_2$ and $K_d = 47\ nM$ and n=1.55 for PI(3,4)$P_2$. The black lines represent the fitted regression model, and the dashed black lines represent the bounds of the 95% confidence interval. **(E)** Representative fluorescent image used for quantifying the sorting ratio of SNX9 from membrane tubes pulled from GUVs containing either PI(3,4)$P_2$ or PI(4,5)$P_2$. **(F)** Sorting ratio as a function of inverse tube radius for GUVs containing either PI(3,4)$P_2$ (green) or PI(4,5)$P_2$ (orange).

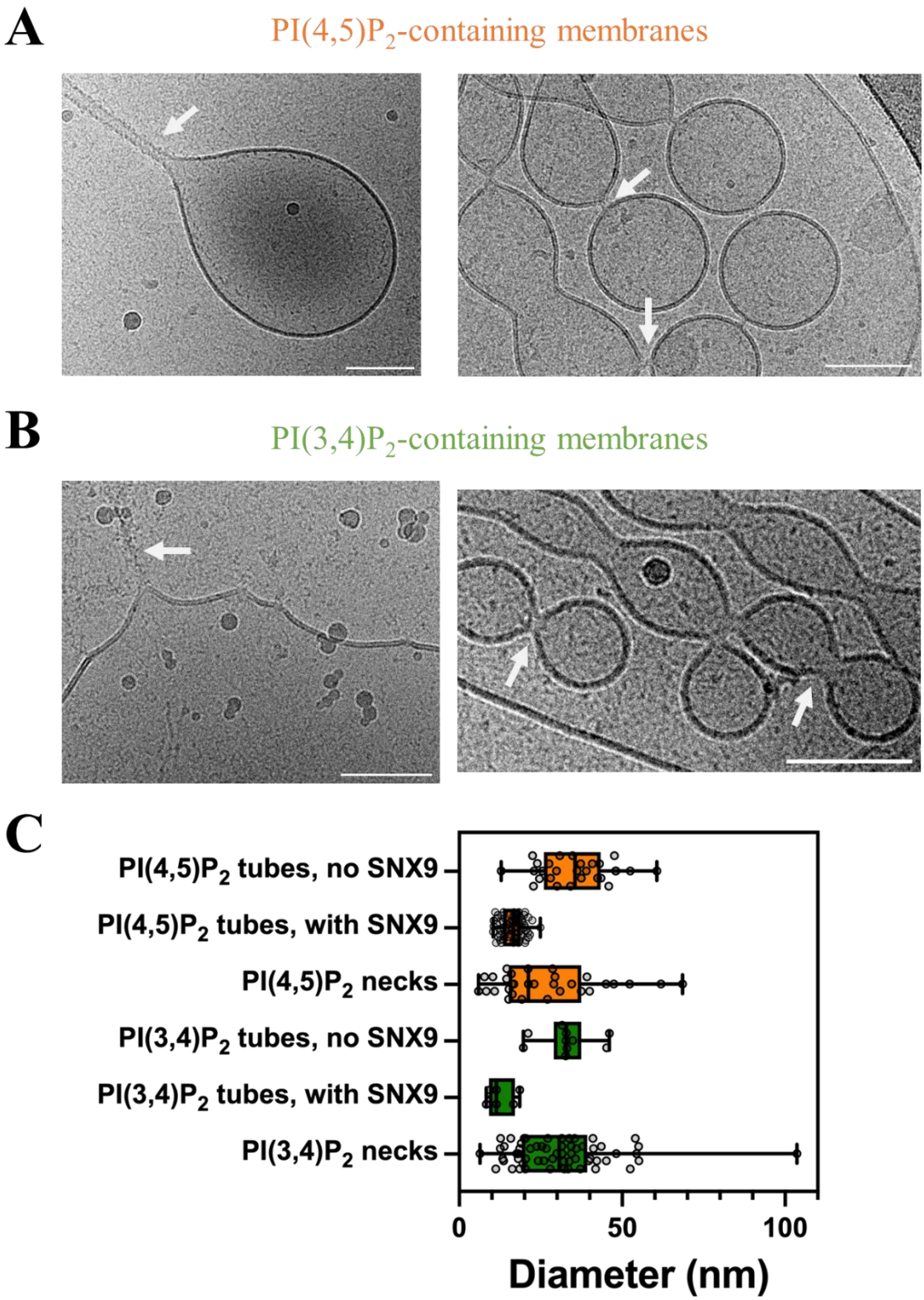


**Figure 4:** SNX9 induces remodeling and membranes containing either $PI(3,4)P_2$ or $PI(4,5)P_2$. Representative images from cryo-EM imaging of full length SNX9 incubated with membranes containing $PI(4,5)P_2$ **(A)** or $PI(3,4)P_2$ **(B)** of tube and neck-like structures indicated by the white arrows.. Scale bar, 100 nm. **(C)** Quantification of the diameters of observed membrane structures, including tubes with no apparent SNX9, tubes with apparent SNX9 signal, and neck-like structures with apparent SNX9 signal.

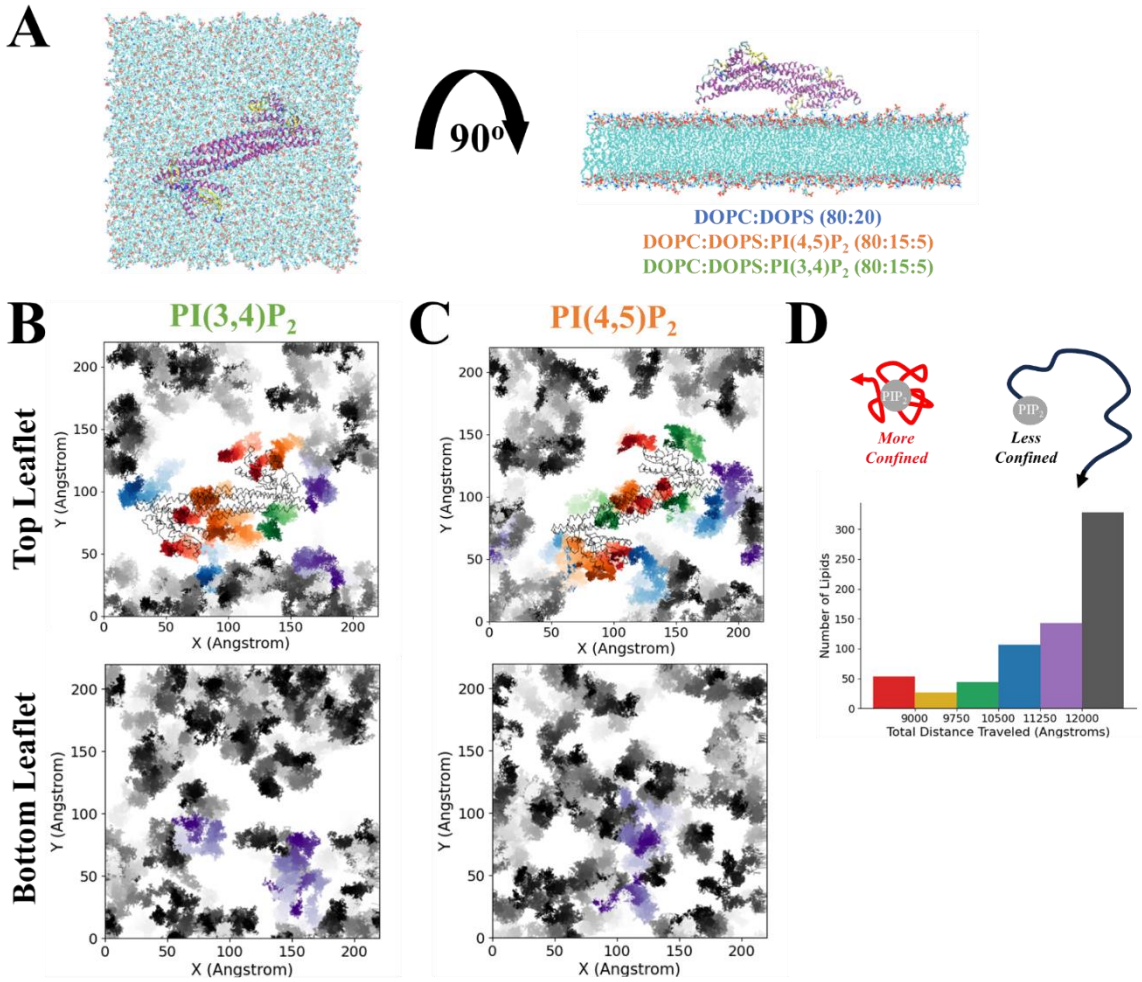


**Figure 5:** SNX9-PXBAR locally changes $PIP_2$ lipid behavior in atomistic molecular dynamics simulations. **(A)** Top (left) and side (right) views of the initial simulation set up. The membrane is shown in a point style colored by atom type, while the SNX9-PXBAR domain is represented in a cartoon style colored by secondary structure. Visualization performed with VMD. **(B)** Representative trajectory trace of the last 750ns (from 1µs trajectory replicate) of the $PI(3,4)P_2$ lipids in the upper (top) or lower (bottom) membrane leaflet, colored by total distance traveled. Average position of the SNX9-PXBAR are shown in wire representation on the upper leaflet. **(C)** Representative trajectory trace of the last 750ns (from 1µs trajectory replicate) of the $PI(4,5)P_2$ lipids in the upper (top) or lower (bottom) membrane leaflet, colored by total distance traveled. Average position of the SNX9-PXBAR are shown in wire representation on the upper leaflet. **(D)** Histogram of total distances traveled over all replicates for both $PI(3,4)P_2$ and $PI(4,5)P_2$ lipids, with bars colored to match trajectory trace colorations in (B) and (C) as well as in Supplementary Figures 1-4.

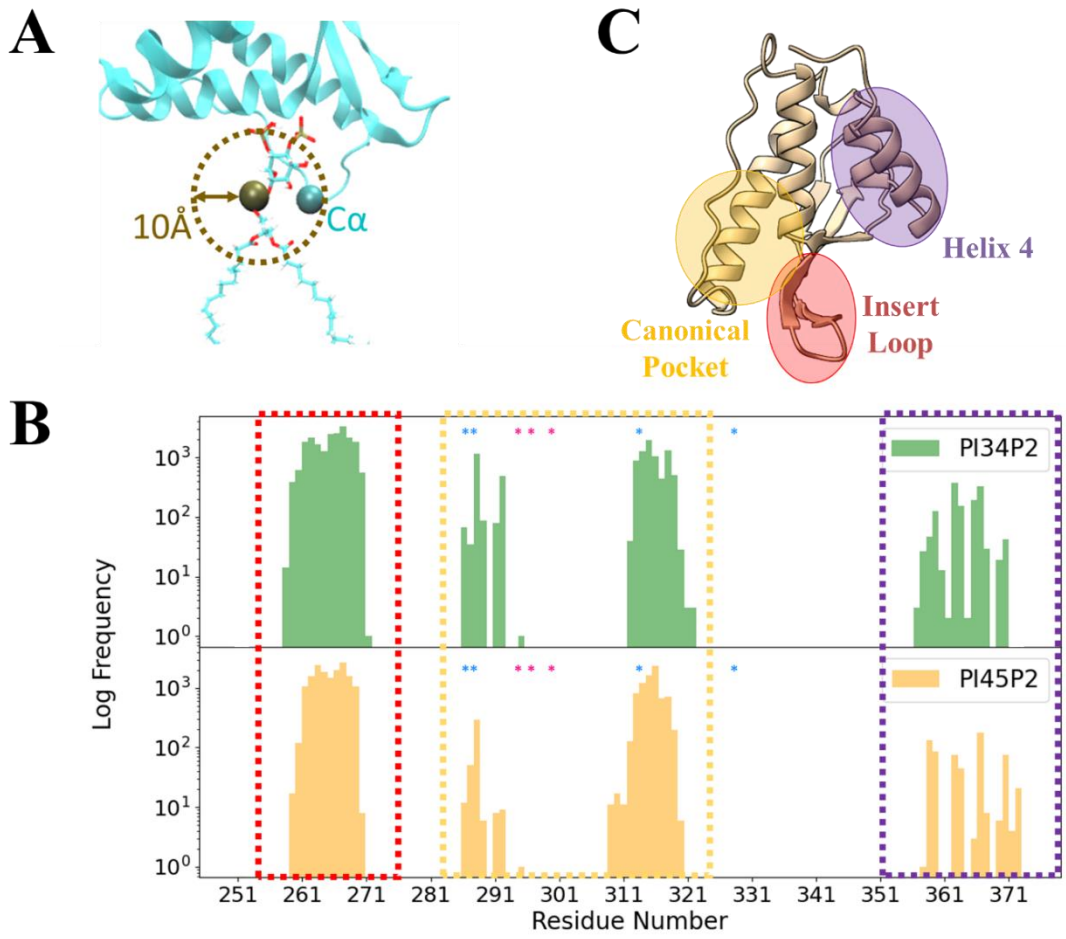


**Figure 6:** Distinct $PIP_2$ binding interfaces of the PX domain can be identified from atomistic molecular dynamics simulations of the SNX9-PXBAR interacting with membranes containing either $PI(3,4)P_2$ or $PI(4,5)P_2$. **(A)** Metric for calculating interactions. If the alpha carbon of a residue is within 10 Å of the central phosphorus of a $PIP_2$ lipid, the two are considered as interacting during that frame of the simulation. **(B)** Tabulated log frequencies of interactions for PX domain residues shows clear groupings corresponding to membrane binding areas, designated as the insertion loop (red), the canonical pocket (yellow), and the fourth helix (purple). Blue stars designate canonical binding residues and pink stars designate additional conserved residues identified via homology, according to *(11)*. **(C)** Cartoon depiction of the SNX9-PX domain, with approximate membrane binding areas highlighted with ovals; colors correspond to the boxes outlined in (B).

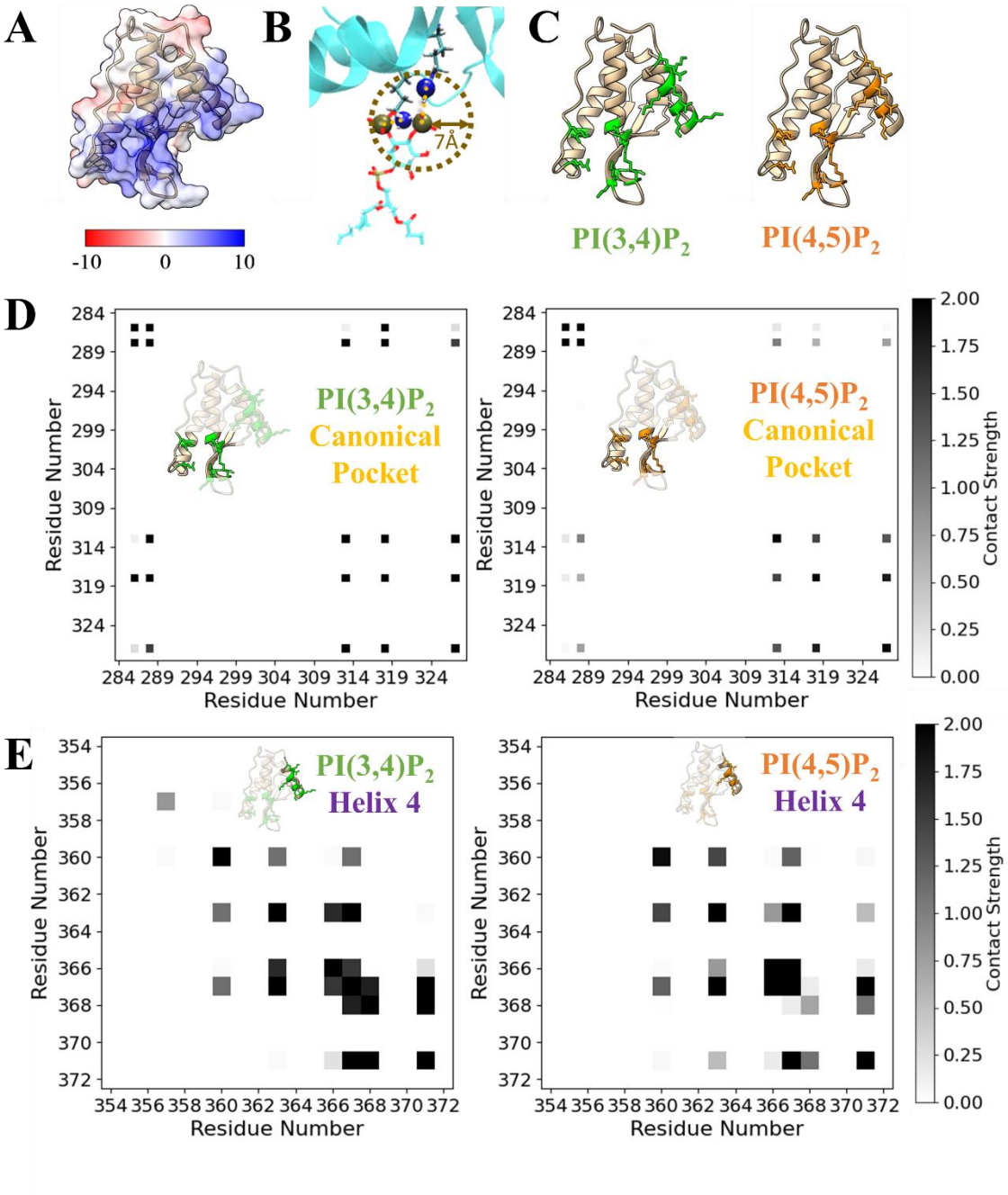


**Figure 7:** Electrostatics play a primary role in PX/$PIP_2$ interactions, particularly in the helix four subdomain. **(A)** Cartoon and electrostatic surface representation of the SNX9-PX domain, with blue indicating positively charged regions and red indicating negatively charged regions. **(B)** Illustration of Bjerrum metric, where a side chain nitrogen atom from an arginine or lysine residue within 7 Å of a $PIP_2$ phosphate group was considered as interacting. **(C)** Cartoon representations of the SNX9-PX domain, with super self-coordinating residues for PI(3,4)$P_2$ (left) and PI(4,5)$P_2$ (right) highlighted in green and orange (respectively) with side chain stick representations. **(D)** PX domain interaction networks for PI(3,4)$P_2$ interactions (left) and PI(4,5)$P_2$ interactions (right). The subdomains designated in Figure 4 are outlined to highlight the interactions within a subdomain as well as interdomain contacts. **(E)** Fourth helix of the PX domain interaction networks for PI(3,4)$P_2$ interactions (left) and PI(4,5)$P_2$ interactions (right).

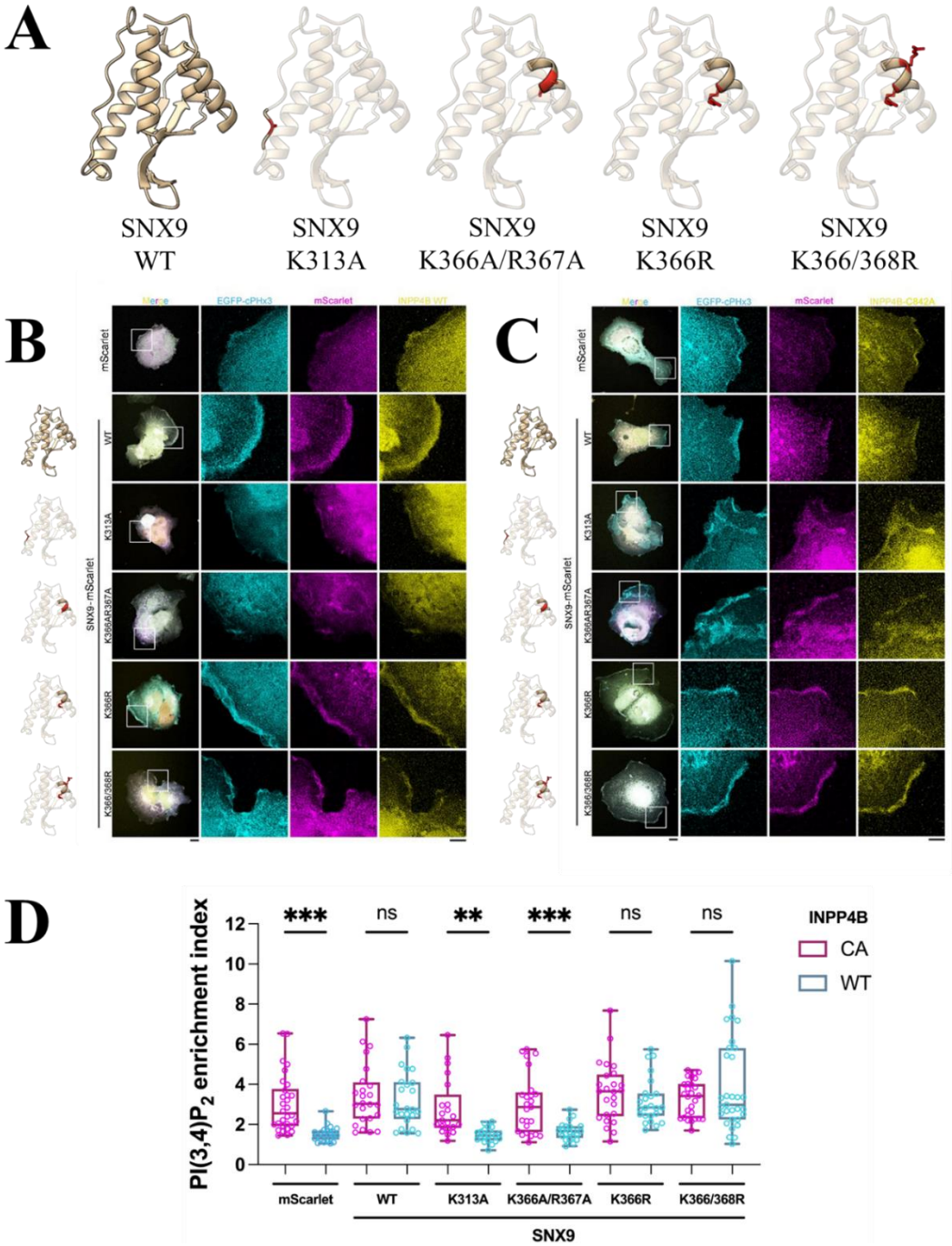


**Figure 8:** Mutations in the SNX9 PX domain impacts its protective effect on PI(3,4)$P_2$ hydrolysis at membrane ruffles. **(A)** Cartoon representations of PX domain, with mutations emphasized by highlighting the affected residue in red and showing the new sidechain. **(B)** Wild-type or **(C)** catalytically dead INPP4B-CAAX (CA) and PI(3,4)$P_2$ reporter were co-transfected into cells together with SNX9-mScarlet or empty vector. After 24 hour incubation in culture medium, cells were fixed and imaged with z-stack confocal microscopy. Projected images are shown. **(D)** PI(3,4)$P_2$ enrichment index. The enrichment level of PI(3,4)$P_2$ is derived by quantifying the fluorescent intensity fold change at plasma membrane between ruffle and non-ruffle area. Each dot represents one cell. PI(3,4)$P_2$ enrichment index in cells expressing indicated SNX9-mScarlet variant together with WT-INPP4B or CD-NPP4B were quantified and compared. Data are analyzed with one-way ANOVA. ***, $p < 0.01$; ****, $p<0.001$.